

# Chapter 3

## The LHCb experiment

### Contents

---

<b>3.1 CERN and the LHC . . . . .</b>	<b>5</b>
3.1.1 The accelerator complex . . . . .	6
3.1.2 Beam conditions . . . . .	8
<b>3.2 The LHCb detector . . . . .</b>	<b>9</b>
3.2.1 Magnet . . . . .	11
3.2.2 Vertex Locator . . . . .	12
3.2.3 Silicon Tracker . . . . .	16
3.2.4 Outer Tracker . . . . .	18
3.2.5 Ring imaging Cherenkov detectors . . . . .	20
3.2.6 Calorimeters . . . . .	24
3.2.7 Muon system . . . . .	27
3.2.8 Trigger . . . . .	29
3.2.9 Reconstruction . . . . .	32
<b>3.3 Luminosity determination . . . . .</b>	<b>34</b>
3.3.1 Van der Meer scans . . . . .	35
3.3.2 Beam gas imaging . . . . .	36

---

This chapter describes the LHCb experiment; including both the accelerator complex responsible for providing  $pp$  collisions and the LHCb detector itself. The LHCb experiment is a collaboration of around 800 scientists from 72 different institutions in 16 countries. The primary physics goals are to look for indirect signs of New Physics by searching for sources of  $CP$  violation and searching for rare decays of  $b$ -

and  $c$ -hadrons. The experiment is situated on the Large Hadron Collider at CERN, Geneva.

### 3.1 CERN and the LHC

In the aftermath of the Second World War a number of eminent scientists proposed the creation of a collaborative European laboratory dedicated to the study of atomic physics. With this, the ‘Conseil Européen pour la Recherche Nucléaire’ was born; a provisional council set up in 1952 to oversee the laboratory’s creation. The organisation as it is today was established in 1954, renamed the ‘Organisation Européenne pour la Recherche Nucléaire’, although the acronym CERN remained. The purpose of CERN was clear; the convention dictates that the organisation ‘*shall provide for collaboration among European States in nuclear research of a pure scientific and fundamental character*’. Since then CERN has been a hub of fundamental nuclear and particle physics research, producing a number of Nobel Prize-winning discoveries, alongside technological developments benefiting society as a whole.

The convention stipulates that the organisation ‘*shall have no concern with work for military requirements*’ and requires ‘*the results of its experimental and theoretical work shall be published or otherwise made generally available*’. The choice of the laboratories location followed a similar set of values, picking Geneva, Switzerland owing both to the central European location and neutrality of the host state.

Perhaps the most well known accelerator in the complex, CERN is home to the Large Hadron Collider (LHC). Two beams of hadrons circulate in opposite directions around 27 km rings, colliding at four interaction points. The beam pipes and experimental halls are buried deep underground, providing shielding from cosmic radiation and reducing the cost of acquiring large areas of land. The tunnels traverse the Franco-Swiss border at a depth that varies between 50–175 m at the lowest and highest points respectively.

The tunnel and caverns occupied by the LHC pre-date the current accelerators and experiments. There were originally constructed for the Large Electron Positron

Collider (LEP). This machine began operation in 1989 and collided electrons and positrons at a collision energy of  $\sqrt{s} = 209$  GeV.

### 3.1.1 The accelerator complex

The LHC is only one of a vast collection of accelerators at CERN, albeit the largest. The hadrons collided in the LHC travel sequentially through a number of different machines, boosting their energy in each. The full complex is shown in Fig. 3.2 along with a legend detailing the types of particles considered. The protons begin life in a hydrogen gas canister. The gas is ionised and accelerated in a linear accelerator, LINAC2, to an energy of 50 MeV. These then pass into the Proton Synchrotron Booster, raising the energy further from 50 MeV to 1.4 GeV.

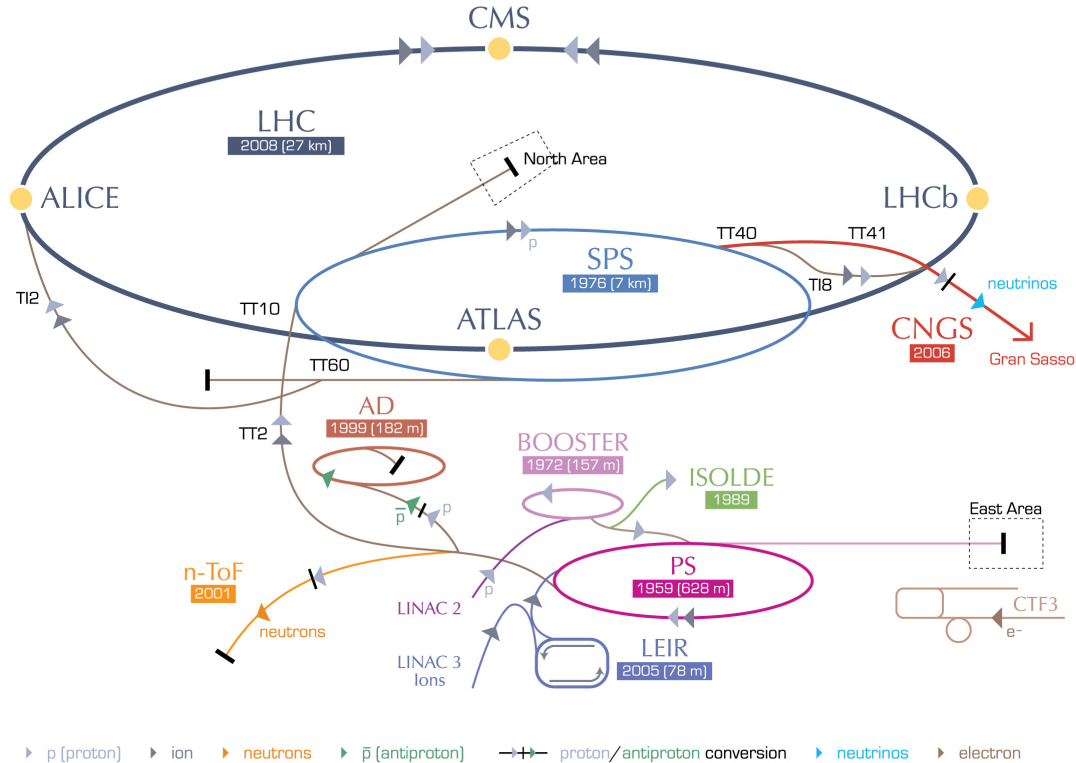


Figure 3.1: The accelerator complex at CERN.

In addition to protons, the complex can accelerate other ions including lead, and more recently, xenon. These start in a dedicated linear accelerator, LINAC3, where the electrons are stripped off the ions to produce bare nuclei before being injected

into the Low Energy Ion Ring (LEIR). This ring raises the ion's energy from 4.2 MeV to 72 MeV.

Either protons or ions can then be injected in the Proton Synchrotron (PS), CERN's first synchrotron. Once the world's highest energy particle accelerator, this now accelerates the particles up to 25 GeV ready to be injected into the Super Proton Synchrotron (SPS). The SPS is the second largest accelerator at CERN, with a circumference of 7 km. It was switched on in 1976 and resulted in the notable discoveries of the  $W$  and  $Z$  bosons. Here, the particles are finally accelerated up to an energy of 450 GeV, ready for injection into the LHC. The particles are transferred from the SPS to the LHC via two lines, one for each of the LHC beam directions. The two beams, referred to as Beam 1 and Beam 2, travel clockwise and anti-clockwise respectively when viewed from above. Beam 2 is injected just before the LHCb detector.

The particles travel through the accelerator complex in groups called bunches. These typically contain around  $10^{11}$  protons and are necessary as a result of the Radio-frequency (RF) cavities that accelerate the particles. The bunches are sequentially transferred between the accelerators in collections called trains. The bunch-trains are transferred from the SPS to the LHC in a series of injections. Although the LHC has a capacity for 3465 bunches, the nominal operating conditions has only 2808 of these spaces filled. These extra gaps allow enough room to safely divert the direction of the beam, without unintentionally damaging the instrumentation around the beam-pipe. The turn-on time for the magnets responsible for dumping the beam in emergencies is longer than the nominal 25 ns bunch spacing.

Once the LHC is at capacity the beams are accelerated from the injection energy of 450 GeV to the nominal energy of up to 7 TeV. This is achieved using eight RF cavities per beam to increase the beam energies and 1232 superconducting dipole magnets that bend the trajectory of the charged particles, ensuring they follow the paths dictated by the circular tunnels. The 15 m long dipole magnets contain superconducting niobium-titanium cables, kept cool at 1.9 K using super-fluid helium. The 11,850 A current flowing through the magnets generates a large magnetic field of 8.33 T. The current

is gradually and synchronously ramped as the particles are accelerated, such that the same curvature trajectory is maintained.

The LHC contains a wealth of other magnets, another 8,361 in addition to the dipole magnets, that optimise the orbit of the beams. These ensure the beams remain tightly packed together, as well as correcting many higher order perturbations.

During the injection and acceleration phase no collisions take place. Once the beams are at the nominal energy and profile distribution have been optimised, the two beams are brought together at four interaction points around the ring. Magnets are used to both redirect the beams such that they crossover and to squeeze the beams to a smaller cross-section at the collision points, increasing the likelihood of collisions. Once the beams overlap and the particles collide the experiments located around the four interaction points can begin to record data. The collisions typically continue for a duration of 10–20 hr (referred to as a fill). The number of particles in the bunches reduce, or *burn-off*, as they collide with one another and the beam-pipes. A fill ends when the beams are intentionally dumped, when the number of protons in each bunch gets too low, or unintentionally dumped, to ensure the safety of the machine. The beam dumps are large graphite blocks surrounded by concrete shielding, designed to absorb the energy of the beams.

A total of seven experiments are located at the LHC, situated in four caverns. The four largest are ATLAS, CMS, LHCb and ALICE. The TOTEM, LHCf and MoDEL experiments are located in the same caverns as CMS, ATLAS and LHCb respectively.

### 3.1.2 Beam conditions

The beam conditions at the LHC have varied between the different years of data taking included in this thesis. A summary of some key parameters are detailed in Table 3.1. This also includes the nominal conditions for the LHC, for which it was designed.

During a normal fill the luminosity delivered to the large experiments slowly decreases as the protons burn off. For ATLAS and CMS the average number of collisions

Condition	2011	2012	2015	2016	Nominal
$\sqrt{s}$ ( TeV)	7	8	13	13	14
Peak luminosity ( $10^{33} \text{ cm}^{-2} \text{ s}^{-1}$ )	3.5	7.6	4.8	14	12
Bunches	1380	1380	1368	2736	2808
Bunch spacing ( ns)	50	50	25	25	25
Average $N_{\text{collisions}}$ , $\mu$	1.7	1.7	1.1	1.1	-
Integrated luminosity ( $\text{fb}^{-1}$ )	1.0	2.0	0.3	1.5	-

Table 3.1: Beam conditions in the different datasets used in this thesis. The last two rows are specific to LHCb.

per bunch crossing (known as pile up) is high: around 27 in 2016. The LHCb experiment chooses to level the luminosity to a lower value than the maximum achievable. This means the average number of visible collisions per bunch crossing,  $\mu$ , is much lower, between 1.1 and 1.7 depending on the year. The same luminosity is maintained for the majority of a fill via a process known as luminosity levelling. At the beginning of the fill the two beams are vertically separated from one another such that the overlap between them is not maximised. As the fill progresses the two beams are brought closer together to compensate for the burn off of the bunches. This way a constant instantaneous luminosity of between  $(2\text{--}4)\times 10^{32} \text{ cm}^2 \text{ s}^{-1}$  can be maintained throughout the given fill.

In addition to the luminosity levelling, the two beams collide at an angle in the horizontal plane. This helps to reduce unwanted collisions between the bunches either side of the intended collision bunches. The angle of collision depends on the polarity of the LHCb spectrometer magnet as the dipole field affects beam-steering fields around the interaction point.

## 3.2 The LHCb detector

This section provides an overview of the experimental apparatus used to obtain the data analysed in this thesis. The LHCb detector is comprised of distinct sub-detectors, each with a dedicated purpose. These help to characterise the sub-atomic particles created in the proton-proton collisions, and enable measurements of their kinematics,

trajectories and species. This overview includes a description of the sub-detector's principles, components and performance.

The LHCb detector is found at Point 8 of the LHC ring, in a cavern originally built for the DELPHI detector during the LEP era. A schematic representing the key components of the LHCb detector is shown in Fig. 3.2. This figure displays the axes convention adopted by LHCb, and used henceforth. The horizontal axis is labelled the  $z$ -axis and is parallel to the direction of the beams. The figure's vertical axis is the  $y$ -axis, increasing as one moves from the cavern up to ground level. The  $x$ -axis is in the dimension perpendicular to the plane of the figure and increases as one moves towards the centre of the LHC ring. The counter-rotating beams of protons are collided at the far left of this figure, at the origins of the  $y$ - and  $z$ -axes.

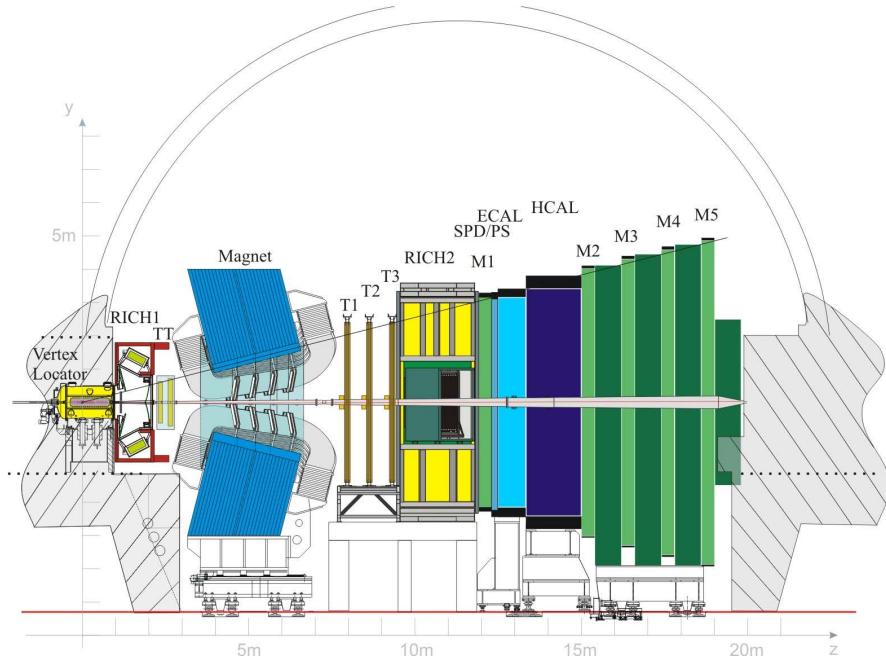


Figure 3.2: Schematic of the LHCb detector, from Ref. [2].

The LHCb detector covers only a small fraction of the area around the collision region; the acceptance covers particles with a pseudo-rapidity in the range  $1.8 < \eta < 4.9$  on one side of the interaction point. However, this configuration is well suited to the reconstruction of particles containing  $b$  or  $\bar{b}$  quarks. The angular distribution of  $b\bar{b}$  pairs is shown in Fig. 3.3, along with the acceptance of LHCb in red. The

distribution is highly peaked towards the forward and backward regions as  $b$ -hadrons tend to receive large boosts at this collision energy. Approximately 25% of decays have both  $b$  and  $\bar{b}$  quarks produced inside the acceptance.

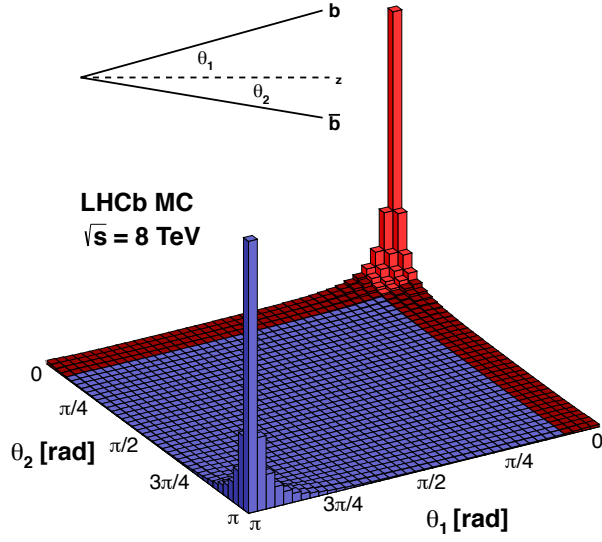


Figure 3.3: The angular distribution of  $b\bar{b}$  pair production in simulated  $pp$  collisions at a centre-of-mass energy of 8 TeV. The acceptance of LHCb is highlighted in red.

Running along the centre of the detector is the LHCb beampipe. The primary role is to separate the inner vacuum chamber from the rest of the cavern, allowing the beams to proceed unimpeded by the air. The majority of the beampipe is made of beryllium, with smaller sections made out of aluminium alloys or stainless steel. Although beryllium is a highly toxic and fragile material it has a long radiation length, allowing the incident particles to traverse the pipe walls with minimal interactions.

### 3.2.1 Magnet

The LHCb detector contains a warm dipole magnet that bends the trajectories of charged particles, allowing measurements of the particles' momentum. The magnet has two saddle-shaped coils inside a square yoke that generate an integrated magnetic field of 4 Tm. The magnetic field is aligned along the  $y$ -axis, bending the charged

particles in the horizontal plane. The polarity of the magnet is routinely switched during data taking. This helps to understand and cancel systematic effects that may affect measurements of  $CP$  asymmetries. The two magnet polarities are referred to *MagDown* and *MagUp*, corresponding to a field in the negative and positive  $y$ -axis direction respectively.

A schematic of the magnet is shown in Fig. 3.4, along with the strength of the magnetic field as a function of the  $z$ -axis position. Both magnet polarities are represented in this figure.

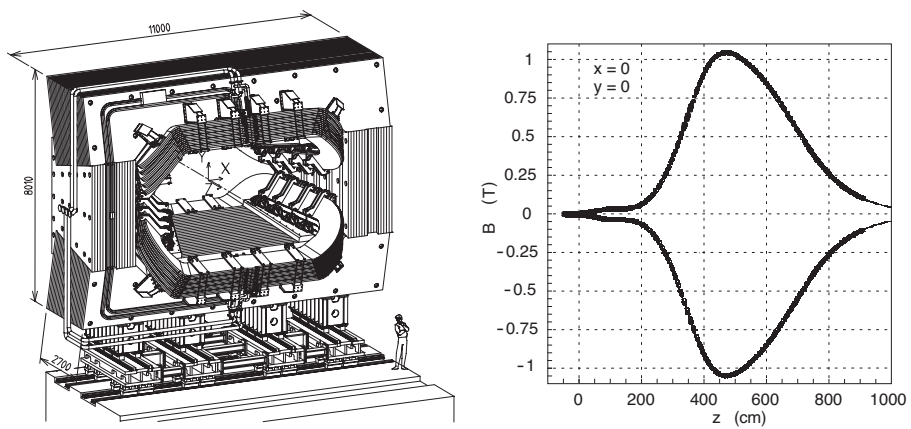


Figure 3.4: Schematic of the LHCb warm dipole magnet (left) and the magnetic field strength along the  $z$ -axis (right) from Ref. [2].

### 3.2.2 Vertex Locator

The first sub-detector to make measurements of the particles produced in proton-proton collisions is the Vertex Locator (VELO) encompassing the collision region. This sub-detector makes precise measurements of the track positions of charged particles as they emanate out of the collisions. A high level of precision is required to identify the secondary vertices characteristic of  $b$ - and  $c$ -hadron decays. These secondary vertices are typically displaced from the interaction position as a result of the long lifetimes associated to these heavy-flavour hadrons. This is achieved by measuring the track coordinates using silicon strip sensors placed as close to the LHC beam as safety allows. The VELO sensors are semicircular devices placed on either side

of the beam. To allow the sensors to instrument the innermost region around the interaction point the two halves of the VELO can move horizontally in and out. During normal data taking this allows the sensors to be 7 mm away from the interaction point yet still be a safe distance away from the beams at injection.

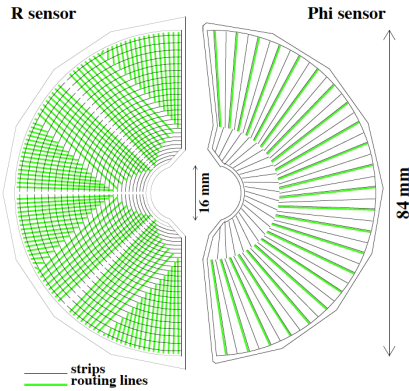


Figure 3.5: Schematic of an  $r$ - and  $\phi$ -sensor in the VELO sub-detector, from Ref. [3].

The sensors are grouped into pairs, called modules. Each of the 21 modules on each side contains sensors for measuring the radial and azimuthal coordinates of the tracks, referred to as  $r$ - and  $\phi$ -sensors respectively. A schematic of the two sensor types is shown in Fig. 3.5, illustrating the silicon strips and readout channels.

The VELO modules are arranged to ensure coverage of particles emerging in forward region at angles of 15–300 mrad with respect to the beam-pipe. This arrangement allows tracks within this acceptance to interact in at least three sensors as shown in Fig. 3.6. The modules extend both forward and backwards of the interaction region. Although momentum measurements are not possible for backward tracks, the vertexing of the primary interaction can benefit from this extra information. In the far backward region there are two additional modules, measuring only the radial coordinate. These help to identify pile-up events in which there is more than one primary vertex.

The VELO sub-detector is constructed to operate in the unique environment close to the LHC beams.

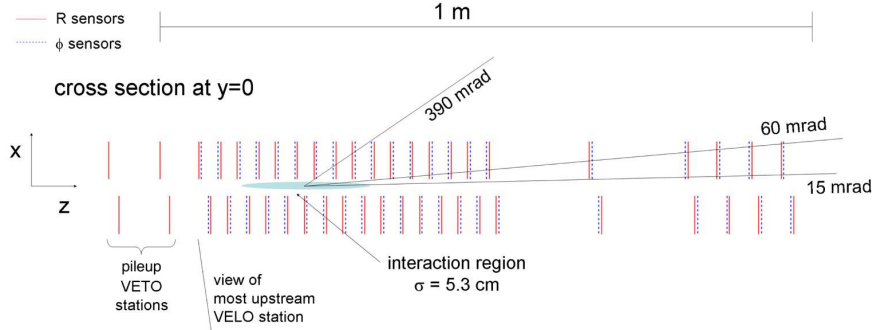


Figure 3.6: Schematic of the sensor layout in the VELO sub-detector, from Ref. [3].

**Radiation resistance:** the VELO modules are subjected to extreme and varying amounts of radiation. The detector is designed to withstand three years of nominal LHC running, using a radiation tolerant semiconductor construction. Additionally, the VELO modules are cooled to remove the heat created from the interactions. The sensors are maintained at a temperature between -10 and 0°C with 24 W of heat removed from each sensor.

**Radio-frequency (RF) pick-up protection:** the electromagnetic fields generated by the LHC beams could cause interference in the VELO detectors electronics. Therefore, a shield is used between the modules and the beam-pipe referred to as the RF-foil. This 0.3 mm thick foil separates the VELO and beam-pipe vacuums, providing additional protection to the conditions of the beams from the detector.

The hits arising from particle interactions in the VELO sensors are extracted from the readout channels using custom analogue chips. The signals are digitised and combined into clusters in readout boards called TELL1 boards [4],

The performance of the VELO sub-detector can be quantified using different metrics. Two of particular interest are the track finding efficiency and the resolution of the impact parameter of a track. The track finding efficiency determines the likelihood that a track will be reconstructed and is of particular importance for high multiplicity final states including those presented in this thesis. The average track

finding efficiency in data taken during 2011 is found to be around 98% as shown in Fig. 3.7.

The impact parameter (IP) represents the distance between a track and a primary vertex at the point of closest approach. Long-lived particles, such as  $B^+$  mesons, decay at a secondary vertex displaced from the primary collision vertex. Therefore, the decay products of these particles have a larger IP than the tracks originating at the primary vertex. A precise measurement of the IP of a track allows the  $B^+$  mesons and various background processes to be differentiated. The distribution of the  $x$ -component of the IP is shown as a function of the inverse transverse momentum ( $1/p_T$ ) in Fig. 3.7.

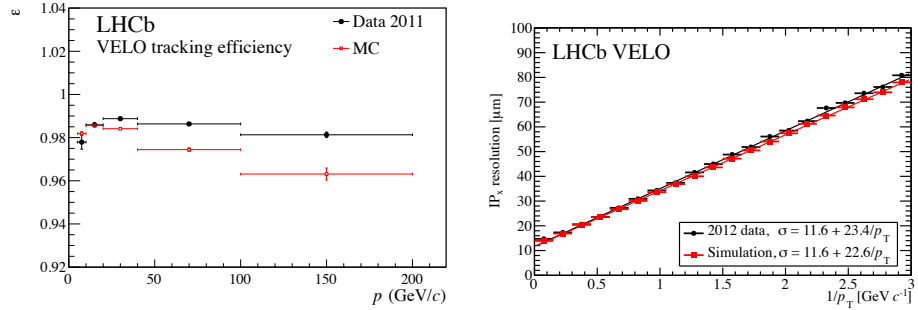


Figure 3.7: The tracking efficiency (left) and  $\text{IP}_x$  resolution (right) in simulation and data, from Ref. [3].

The VELO is situated in a harsh environment, therefore the components gradually degrade as exposed to more and more radiation. The damage to the silicon sensors is monitored over time to ensure the sub-detector is operational and to estimate the remaining lifetime of the sensors. In between LHC fills current-voltage (IV) scans are performed on the silicon semiconductors, measuring the current leaking as a function of the bias voltage. The evolution of this current in Run I is shown in Fig. 3.8, along with the delivered luminosity. These measurements help to predict what bias voltages will be required by the end of Run II.

A comparison of the IP resolution determined using 2012, 2015 and 2016 data is also shown in Fig. 3.8. Although the resolution is broadly similar between the three years, a slight increase in the resolution is present between Run I and Run II.

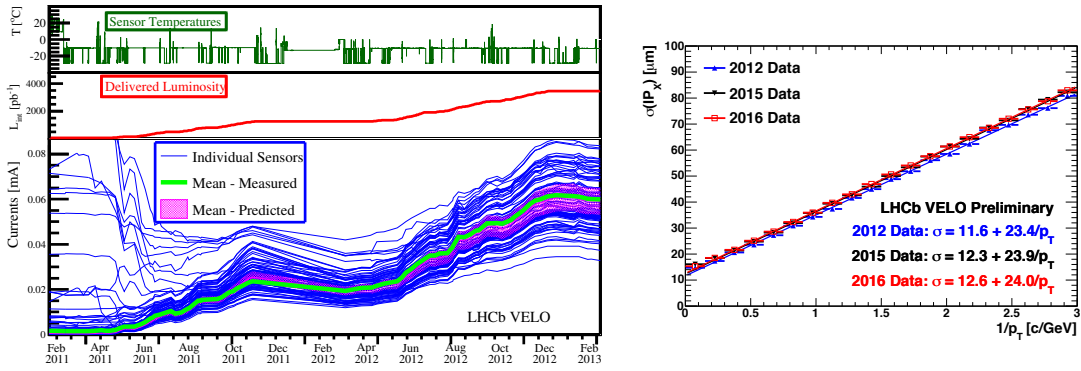


Figure 3.8: The VELO silicon sensor’s leakage current as a function of time through out Run I, from Ref. [5] (left) and the VELO IP resolution in 2012, 2015 and 2016 data (right) . A small decrease in performance is observed between Run I and Run II.

### 3.2.3 Silicon Tracker

In addition to the VELO, there are two more sub-detectors that utilise silicon sensors in order to determine tracking information. These are collectively referred to as the Silicon Tracker (ST), which is made up of two trackers; the Tracker Turicensis (TT) and Inner Tracker (IT). The TT is located before the dipole magnet, whereas the IT is positioned after, as show in Fig. 3.2. Although these two detectors are spatially separated, their common silicon mircostrip sensors and electronics warrant considering them together.

The silicon sensors are made up of single-sided  $p^+$ -on- $n$  sensors. The hits are read out via chips at the end of each module. These chips are the same custom analogue chips used in the VELO sub-detector. The signals pass into digitisers and then through optical fibres into TELL1 boards that perform clustering algorithms. Both sub-detectors are cooled to 5°C and their sealed containers flushed with nitrogen gas to prevent condensation.

#### Tracker Turicensis

The TT is positioned before the dipole magnet and covers the entire LHCb acceptance, standing 130 cm tall and 150 cm wide. It is made up of four layers orientated at angles to one another. The first and fourth layers are parallel, with the second and third at

angles  $-5^\circ$  and  $+5^\circ$  to these respectively. The first and second are separated from the third and fourth by 27 cm along the beam axis. The layout of the silicon modules in the TT is shown in Fig. 3.9. The sensors are grouped into *half-modules* that span half of the vertical height of the sub-detector. These are made up of seven silicon sensors and a readout hybrid at the outermost end. The readout electronics are positioned outside of the LHCb acceptance, limiting the amount of multiple scattering due to interactions with the detector material.

The *half-modules* are arranged to prevent any gaps in the instrumentation. The adjacent *half-modules* are offset by 1 cm along the beam axis, allowing the modules to overlap by a few millimetres in the  $x$ -axis.

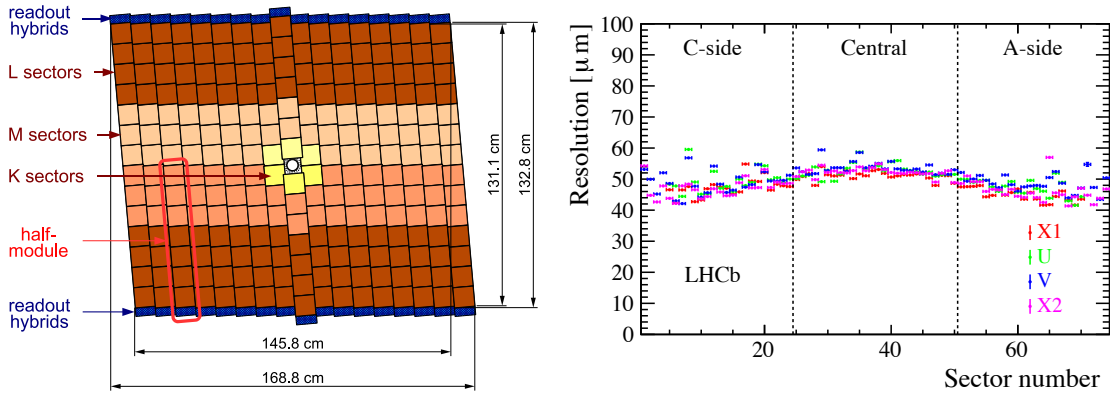


Figure 3.9: Schematic of the TT sub-detector, from Ref. [2] (left) and the TT resolution by sector number, from Ref. [6].

The resolution achieved by the TT is shown in Fig. 3.9, split into different sectors and shown separately for the four layers (labelled X1, U, V and X2). The resolution varies between 40–60  $\mu\text{m}$  and is consistent between the different layers.

### Inner Tracker

The IT is the second silicon detector making up the ST. It is located after the dipole magnet in three tracking stations. As the name implies, it covers only the inner region of the acceptance, measuring 140 cm wide and 40 cm tall, where the particle flux is highest. The rest of the area is covered by the much larger Outer Tracker. Similar to

the TT, the IT is made up of four layers positioned at slight angles to one another. However, as shown in Fig. 3.2, there are three separate IT stations, each containing four layers. These stations are constructed as of four boxes distributed around the beam-pipe in a cross shape, as shown in Fig. 3.10.

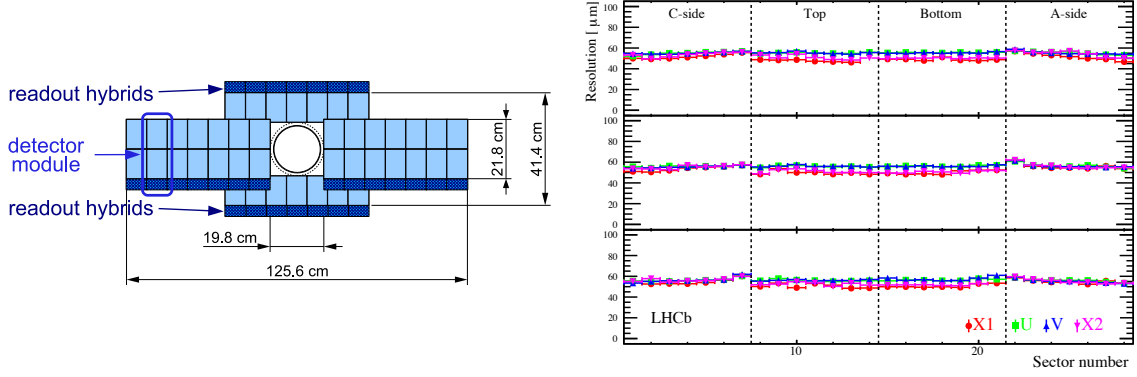


Figure 3.10: Schematic of the IT sub-detector, from Ref. [2] (left) and the IT resolution by sector number, from Ref. [6].

The detector modules consist of either one or two silicon sensors and a readout chip. These are also offset along the beam axis to allow the modules to overlap slightly in the  $x$ -axis.

The resolution of the IT is shown in Fig. 3.10. The resolution is between 40–60  $\mu\text{m}$  and varies between the four different layers.

### 3.2.4 Outer Tracker

In contrast to the the silicon-based sub-detectors already described, the Outer Tracker (OT) is a straw tube tracker filled with a gaseous mixture of argon, carbon dioxide and oxygen. The 4.9 mm diameter straws are 2.4 m in length and arranged in double layers as shown in Fig. 3.11. As with the IT, the OT is split into three stations. Each of these stations similarly has four layers arranged at angles to one another ( $0^\circ, -5^\circ, +5^\circ, 0^\circ$ ). The arrangement of the stations and layers are also shown in Fig. 3.11. The inner region occupied by the IT is visible.

The straws comprising the tracker are composed of an inner wire surrounded by a conducting foil, with a potential difference maintained between the two. When a

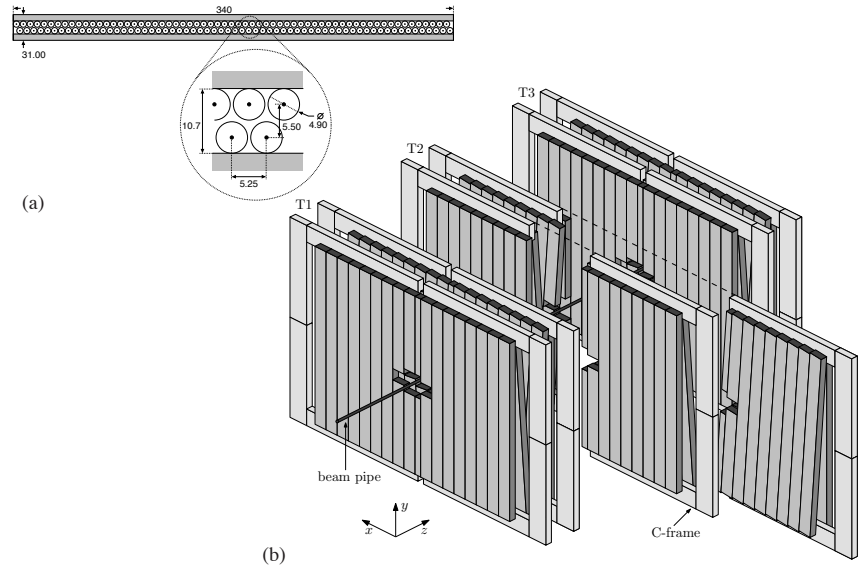


Figure 3.11: Schematic of the OT sub-detector, from Ref. [7].

charged particle passes through the straw the gas becomes ionised. The electrons and gas ions are attracted to the cathode foil and anode wire, resulting in a flow of current. In the OT the inner wire is made of  $25\text{ }\mu\text{m}$  thick gold plated tungsten and maintained at a voltage of  $+1550\text{ V}$ . The surrounding foil is made up of three layers; a  $40\text{ }\mu\text{m}$  thick layer of conducting carbon-doped polyimide film; a  $12.5\text{ }\mu\text{m}$  layer of insulating polyimide; and  $12.5\text{ }\mu\text{m}$  of aluminium.

The double layers of straw tubes as shown in Fig. 3.11 make up a module. Vertically, the modules are split in two, with staggered gaps between the two individual straw layers to avoid an uninstrumented region. Each of the modules are read out from the outermost end. The readout boards contain a number of circuits to process the signals and provide the potential difference to the straw wires. The analogue signals pass through an amplification circuit before being processed and cleaned. These then pass into a digitiser creating a digital value of the drift-time.

The single hit resolution is determined for the OT by determining the width of the hit distance residual distribution. This is shown in Fig. 3.12 giving a resolution of  $205\text{ }\mu\text{m}$ .

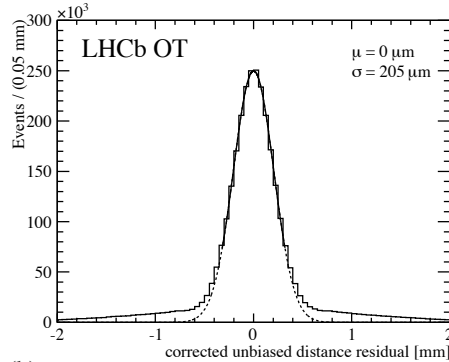


Figure 3.12: The hit distance residuals for the OT, from Ref. [7].

### 3.2.5 Ring imaging Cherenkov detectors

The ring imaging Cherenkov detectors (RICH) provide essential information about the particle identification of tracks, allowing different hadronic species to be distinguished. This allows kaons and protons to be distinguished from one another and the abundant pions tracks in a typical event. It can also help differentiate leptonic tracks in combination with the calorimeters and muon systems.

Two RICH sub-detectors are present, each optimised for particles with different momentums. The first, RICH1, is located between the VELO and TT, before the particles have passed through the magnetic field. This provides discrimination primarily for low momentum tracks between 1–60 GeV/ $c$ . A second sub-detector, RICH2, is located between the IT and OT tracking stations and calorimeters, after the particles have travelled through the magnetic field. This caters for the higher momentum particles in the range 15–100 GeV/ $c$ .

The RICH detectors help to determine the species of the particles passing through it by capturing Cherenkov radiation emitted by the particle as it traverses a transparent medium referred to as a radiator. Cherenkov radiation is produced by particles travelling above the phase velocity of light in that specific medium. The radiation propagates at constant angle  $\theta$  to the particles direction, determined by the speed of the particle  $\beta = v/c$  and refractive index of the material  $n$  as follows

$$\cos \theta = \frac{1}{\beta n}. \quad (3.1)$$

This light is collected by mirrors and focussed onto light sensors.

Although the particles produced in the collisions are all highly energetic and travelling close to the speed of light, the differences in the masses mean the species travel at slightly different velocities. This then results in a different Cherenkov angle. In combination with the momentum measurement from the magnet spectrometer, different mass hypotheses can be compared. The Cherenkov angles for different particle species as a function of momentum are shown in Fig. 3.13.

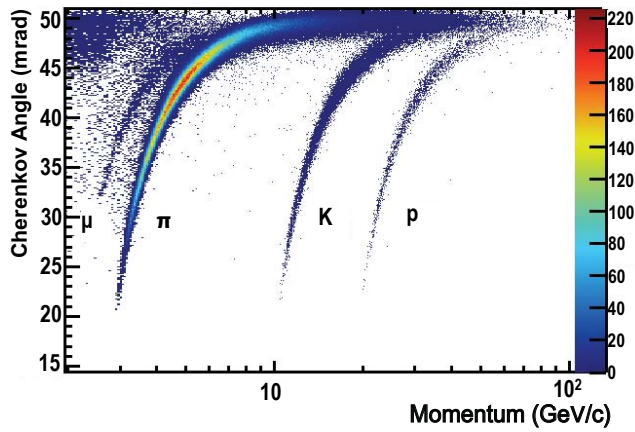


Figure 3.13: The Cherenkov angle for different species of particles as a function of momentum, from Ref. [8].

In both RICH1 and RICH2 the cone of Cherenkov radiation is reflected off spherical and planar mirrors. This not only redirects the radiation onto Hybrid Photon Detectors (HPDs) situated outside of the acceptance but also focusses the radiation into a single ring. The radius of this ring is used to determine the Cherenkov angle  $\theta$ . The identity of particles is determined by comparing likelihood for a given ring of hits to have been created by various species. This is performed globally for all tracks in an event. All tracks are assumed to be pions as these are most abundant. The hypothesis of each is switched to  $e$ ,  $\mu$ ,  $K$  and proton, leaving all other tracks unchanged, and the likelihood recomputed. The species resulting in the minimum value of the global event likelihood is kept. This is repeated until all tracks are set to their preferred hypothesis. The difference in the global event log-likelihood is then

used to indicate the species of each track. Each species is determined relative to the pion hypothesis

$$\text{DLL} = \Delta \log \mathcal{L}(X - \pi) = \log \mathcal{L}(X) - \log \mathcal{L}(\pi), \quad (3.2)$$

where  $\mathcal{L}(X)$  is the global event likelihood when the given track is of the species  $X$ .

### RICH1

The RICH1 sub-detector was designed to aid particle identification for lower momentum tracks in the range 1–60 GeV/ $c$  using two radiators: aerogel and decafluorobutane ( $\text{C}_4\text{F}_{10}$ ). These materials have refractive indices of  $n = 1.030$  and  $n = 1.0014$  respectively for  $\lambda = 400$  nm light. A diagram of the RICH1 detector as seen from the side is shown in Fig. 3.14. To minimise the amount of material that the particles pass through, the RICH1 detector is attached directly onto the VELO exit window.

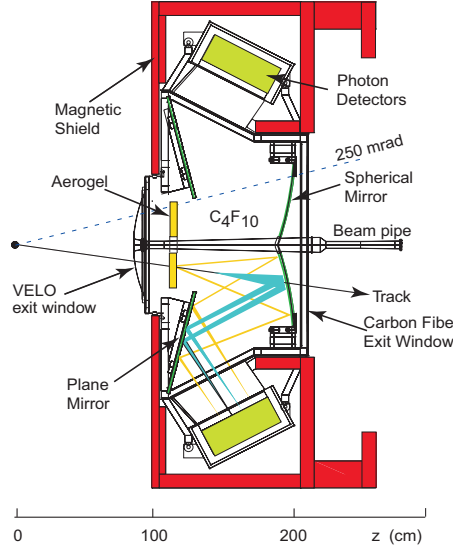


Figure 3.14: Schematic the RICH1 sub-detectors viewed from the side, from Ref. [2].

In Run II the aerogel was removed from the RICH1 detector. Although this catered specifically to the lower momentum tracks, the overall PID efficiency increased [9]. The ability of the aerogel to provide particle identification for kaons below the  $\text{C}_4\text{F}_{10}$  threshold was deteriorated by the number of photons in RICH1 as a result of the high track multiplicity. As well as improving the reconstruction speed,

the removal of the aerogel also allowed full use of the  $\text{C}_4\text{F}_{10}$  gas located between the gel and the VELO entrance window that would otherwise have been blocked.

The single photon resolution for RICH1 is 1.65 mrad, and found to be the same in Run I and Run II.

## RICH2

The RICH2 detector is designed to provide particle identification information for higher momentum tracks in the range 15–100  $\text{GeV}/c$  using a single gas radiator tetrafluoromethane ( $\text{CF}_4$ ). The refractive index for this material is  $n = 1.0005$  for  $\lambda = 400 \text{ nm}$  light.

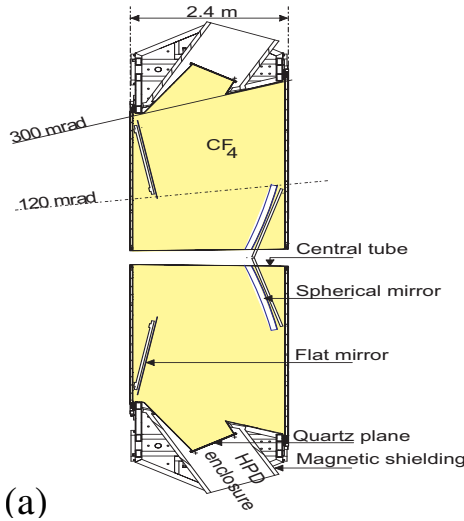


Figure 3.15: Schematic the RICH2 sub-detector viewed from above, from Ref. [2].

The single photon resolution for RICH2 is 0.67 mrad and found to be consistent between Run I and Run II [9].

## Performance

The performance of the RICH detectors can be quantified in terms of the selection efficiency and misidentification rates for different pairs of species. The efficiency of kaon identification and rate of pions being misidentified as kaons is shown in Fig. 3.16 for Run I and Run II. Due to the removal of the aerogel in RICH1, the kaon and pion separation shows a slight improvement in Run II.

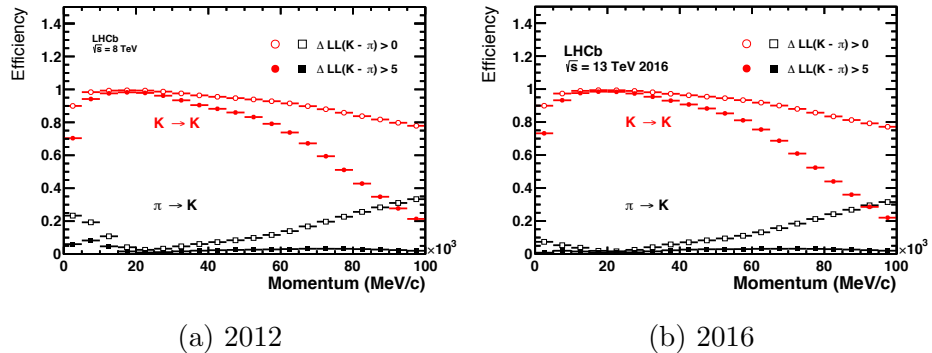


Figure 3.16: The RICH detector performance for kaon and pion separation, from Ref. [8].

### 3.2.6 Calorimeters

The calorimetry system is made of four components that work together to serve a number of purposes. Primarily, the detectors measure energy deposited by particles, vital for neutral pions or photons that don't interact with the tracking stations. Additionally, the calorimeters provide fast measurements of the energy deposited by interacting particles, suitable for use in the trigger. Finally, the four components work together to improve the discrimination of different particle species, in particular between electrons and hadrons.

All of the calorimeter components work on the same basic principle; the particles pass through a transparent materials producing a flash of light, known as scintillation light. This light is collected and measured; the quantity determines the energy deposited by the particle.

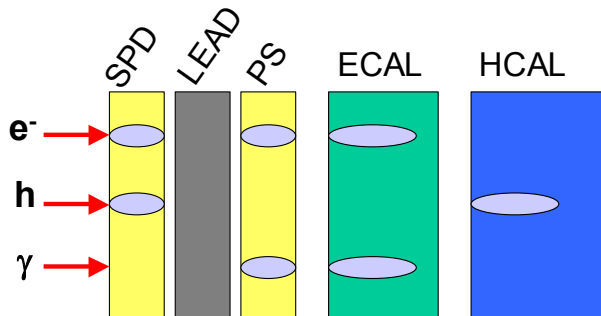


Figure 3.17: A diagram illustrating how the calorimeter system aids particle identification, from Ref. [10].

The first layer of the calorimeter system is the scintillator pad detector (SPD), as shown in Fig. 3.17. This provides information about whether the incident particles are neutral or charged. After this comes the pre-shower detector (PS). This indicates the electromagnetic nature of the particle. For charged particles this separates electrons and charged hadrons; for neutral particle it helps separate photons from neutral hadrons. Next comes the electromagnetic calorimeter (ECAL) tasked with measuring the energy of electromagnetically interacting particles, including electrons and photons. Finally, the hadronic calorimeter (HCAL) determines the energy deposited by hadrons, including pions, kaons, protons and neutrons.

### **Scintillator pad detector and Pre-shower detector**

The SPD and PS are almost identical scintillating pads detectors constructed from a mix of polystyrene and wavelength-shifting dopants. The pads are coated in light-proof paper and contain loops of wavelength-shifting fibres to collect the scintillation light. The pads are segmented into cells, matching the granularity of the ECAL detector. The fibres are connected to long clear fibres connected to photo-multiplier tubes (PMT) outside the detectors acceptance. Between the SPD and PS detectors is a 15 mm thick layer of lead. This layer initiates electrons and photons to interact electromagnetically, depositing some of their energy in the PS scintillating pads.

### **Electronic Calorimeter**

The ECAL is made of 66 layers of alternating lead and scintillator, with a total depth of 42 cm. This thickness corresponds to 25 radiation lengths. The layout of the layers are shown in Fig. 3.18. Scintillating light is captured and transported by wavelength-shifting wires that pass through the entire structure. The light is measured by PMTs positioned at the end of the structure. The cells of the ECAL are segmented differently depending on the proximity to the beam-pipe, as shown in Fig. 3.18. The cells are split into inner, middle and outer regions with sizes  $4 \times 4$  cm,  $6 \times 6$  cm and  $12 \times 12$  cm respectively.

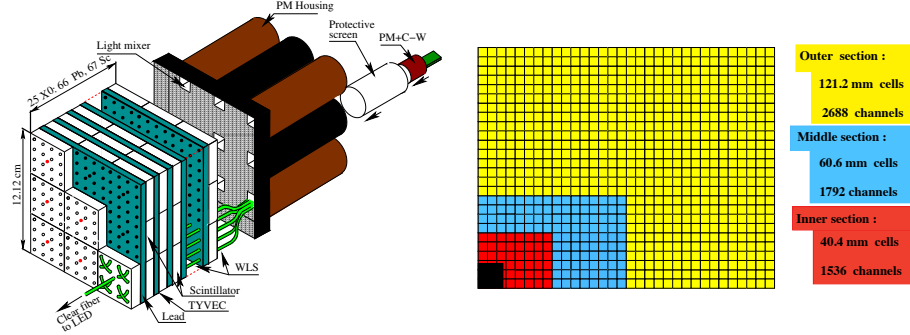


Figure 3.18: A diagram of one of the inner ECAL modules (left) and the layout of one quarter of the ECAL modules (right), from Ref. [2] and Ref. [11].

The resolution of the ECAL can be parametrised as

$$\frac{\sigma_E}{E} = \frac{(8.5 - 9.5)\%}{\sqrt{E}} \oplus 0.8\%, \quad (3.3)$$

where the energy  $E$  is measured in GeV (from Ref. [12]). During data taking the ECAL receives a large dose of radiation. This radiation damages the detector modules as well as the light guides and PMTs. The measurement of irradiation can be quantified by looking at the PMT light yields, as shown in Fig. 3.19. This can be extrapolated to determine the innermost ECAL modules will remain operational for a 13 TeV data set corresponding to an integrated luminosity of  $10\text{--}13 \text{ fb}^{-1}$ .

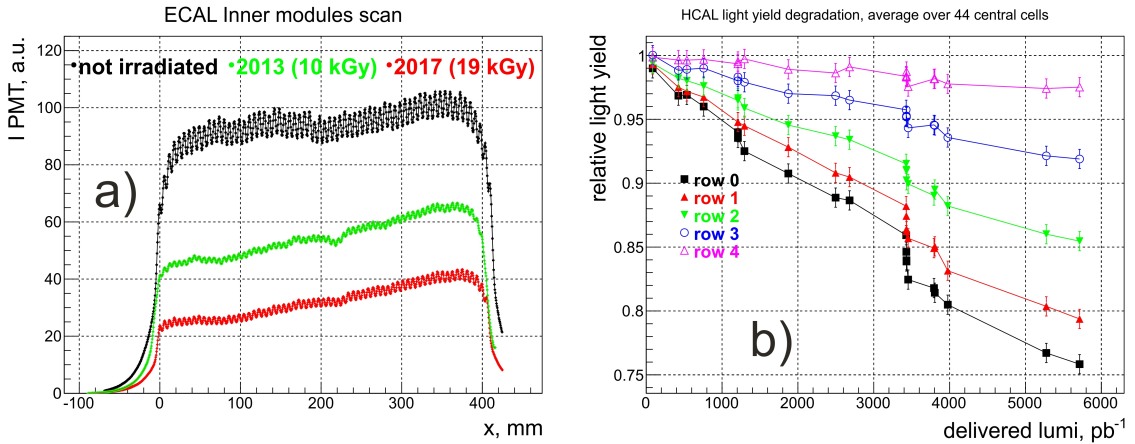


Figure 3.19: The result of radiation damage to the ECAL (a) and HCAL detectors (b), from Ref. [12].

### Hadronic calorimeter

The HCAL is a 500 tonne detector constructed from iron plates and scintillating tiles. Unlike the ECAL, these are arranged parallel to the beam-pipe as shown in Fig. 3.20. The cells vary in size in the different regions of the detector; the inner regions correspond to  $13 \times 13$  cm cells and the outer to  $26 \times 26$  cm. The widths of the iron tiles are chosen to be one radiation length (1 cm), and the lengths are one hadron interaction length. The scintillation light is collected by wavelength-shifting fibres that are read out by PMTs located at the rear of each cell.

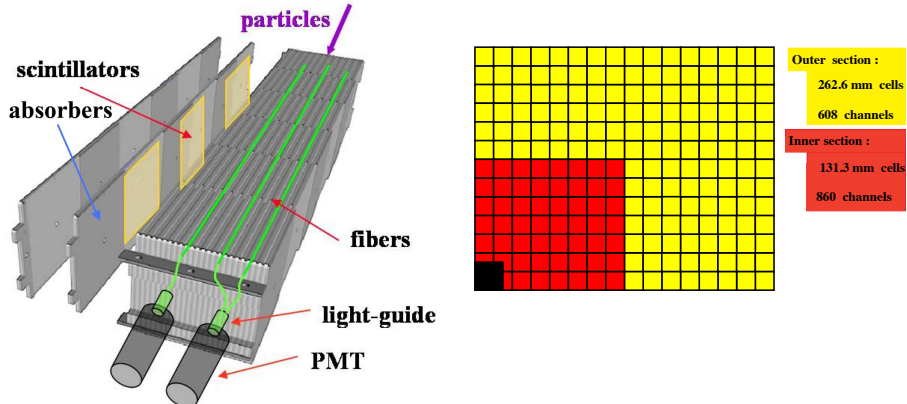


Figure 3.20: A diagram of one of the HCAL modules (left) and the layout of one quarter of the HCAL modules (right), from Ref. [2].

The resolution of the HCAL can be parametrised as

$$\frac{\sigma_E}{E} = \frac{(69 \pm 5)\%}{\sqrt{E}} \oplus (9 \pm 2)\%, \quad (3.4)$$

where the energy  $E$  is measured in GeV (from Ref. [12]). The HCAL receives a large dose of radiation during data taking. This mainly affects the detector modules as the PMTs are located further away from the beam. The decrease in the light yield as a function of the accumulated data set is shown in Fig. 3.19.

### 3.2.7 Muon system

The muon system serves two main purposes: to provide fast muon  $p_T$  measurements for use in the hardware trigger; and to provide muon identification information for

use in the software trigger and offline analyses. The muon system is made of five rectangular stations. The first (M1) is positioned before the calorimeters and the remaining (M2–M4) are positioned after, as shown in Fig. 3.21. The latter stations alternate with 80 cm layers of iron absorbers. The muon system is the last sub-detector as muons are highly penetrating particles, travelling through more material than other species. The interleaving iron absorbers help to isolate muons, as other particles are stopped by these layers.

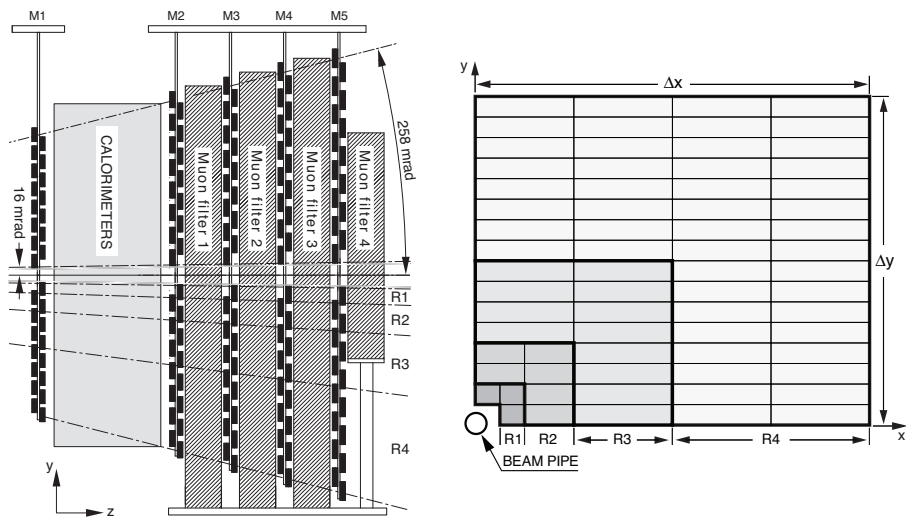


Figure 3.21: Side view of the Muon sub-detector (left) and layout of the muon system regions (right), from Ref. [2].

Each of the stations are divided into four regions R1–R4. These are positioned increasingly further from the beam-pipe with increasingly large areas. Each of the regions are segmented into channels; the inner regions have more segmentation than the outer regions such that the particle flux is roughly constant over the four regions.

The majority of the detector is constructed from Multi Wire Proportional Chambers. These chambers contain a gaseous mixture of carbon dioxide, argon and tetrafluoromethane. When muons pass through this gas they cause ionisation. An array of gold-plated tungsten wires separated by 2 mm are held at a potential difference of around 2.5 kV with respect to the chamber's conductive walls. The ionised gas and electrons are deflected by the electric field and result in a flow of current.

Due to the larger flux of particles, the innermost region (R1) of the first station (M1) is instrumented using triple gas electron multiplier detectors. The muons propagating through these detectors ionise a gas mixture made up of argon, carbon dioxide and tetrafluoromethane. The resulting electrons are accelerated toward an anode through three foil layers. The foil layers multiply the number electrons, creating a cascade. This type of detector was chosen for the inner region as it is required to be especially radiation hard such that the detector can withstand 10 years of operation.

### 3.2.8 Trigger

The primary role of the trigger is to reduce the nominal 40 MHz beam crossing frequency to a more manageable rate that can realistically be recorded. The trigger is composed to two parts: a custom hardware trigger called Level 0 (L0) that operates at the nominal 40 MHz beam crossing rate; and an asynchronous High Level Trigger (HLT) running software algorithms. These two stages reduce the event rate to around 2 kHz, exploiting the characteristics of  $b$ - and  $c$ -hadron decays to preferentially retain signal decays and discard the many uninteresting events.

#### Level 0

The L0 trigger takes input from the muon system, calorimeters and pile-up veto in the VELO. These three systems feed into a single unit to make a global decision about the event. Although the nominal bunch spacing is 25 ns, the L0 decision is made after 4  $\mu$ s. During this time the detector signals are stored in a *pipeline* buffer. Half of this 4  $\mu$ s budget is required for the time-of-flight of the particles and delays in the electronics, leaving the L0 trigger 2  $\mu$ s to reach a decision about each event.

The L0 calorimeter trigger uses input from the SPD, PS, ECAL and HCAL to trigger events. The particles are reconstructed using  $2 \times 2$  cell clusters to calculate the total transverse energy  $E_T$  deposited. The different particle species are inferred by combining the information from the different calorimeter components.

**L0Hadron:** Hadronic deposits are created by finding the highest energy HCAL cluster with a corresponding ECAL cluster in front of it.

**L0Photon:** Photons are created from the highest ECAL deposits with corresponding PS hits.

**L0Electron:** Electrons are created from the highest ECAL deposits with corresponding PS and at least one SPD hit.

If any of these candidates pass corresponding  $E_T$  thresholds, then the trigger fires.

The L0 muon trigger selects the two highest  $p_T$  muons in each of the four quadrant of the muon system.

**L0Muon:** Any of the eight muons can fire this trigger if their  $p_T$  is greater than a threshold.

**L0DiMuon:** Pairs of muons can fire this trigger if the quantity  $p_{T1} \times p_{T2}$  is greater than a threshold.

The third component of the L0 trigger, the pile-up veto, helps to determine how many primary interactions occurred in a given event. Two VELO  $r$ -sensors measure the radii of backward tracks,  $r_a$  and  $r_b$ . For tracks originated at the same vertex the ratio of these is a constant,  $k = r_b/r_a$ . The ratio of hits are compared and events with multiple events can be vetoed.

## High Level Trigger

The HLT is a software trigger comprised of C++ algorithms on a dedicated processing farm. It is further subdivided into two sections: HLT1 and HLT2. The first stage, HLT1, reduces the rate of events by matching L0 deposits to tracks in the VELO and T-stations. The software algorithm performs partial pattern recognition to match the charged particle L0 deposits to track candidates and to ensure that  $\gamma$  or  $\pi^0$  L0 candidates are not associated to tracks. This part of the trigger reduces the L0 output rate (870 kHz) to around 43 kHz. The VELO tracks are used to create vertices with 5 or more tracks. Tracks are accepted if they are consistent with originating at one of these vertices. For events selected with the muon L0 lines, the VELO tracks are extrapolated to the muon stations to form muon candidates. These VELO or muon

candidates are extrapolated to the T-stations (OT and IT) and reconstructed with a Kalman filter [13, 14].

The second stage, HLT2, performs a full event reconstruction, allowing explicit decays to be reconstructed. Many different trigger algorithms are included in HLT2, reconstructing a wide range of decays. Additionally a set of inclusive  $b$ -hadron decay lines exist, exploiting the common characteristics of these decays. These *topological* trigger lines make decisions based on 2-, 3- or 4-body combinations of tracks that can form a partially reconstructed  $b$ -hadron decay. These tracks are required to pass a minimum distance of closest approach requirement with respect to each other. The invariant mass of these tracks would span a large range in the case of additional non-reconstructed particles, so a quantity called the corrected mass is calculated instead:

$$m_{\text{corr}} = \sqrt{m^2 + |p_{T\text{miss}}'|} + |p_{T\text{miss}}'|, \quad (3.5)$$

where  $p_{T\text{miss}}'$  is the missing momentum transverse to the flight direction of the particle, defined by the vector between the PV and 2-, 3-, or 4-body vertex. Requirements are made to  $m_{\text{corr}}$  to ensure the vertex is consistent with a  $b$ -hadron decay. The tracks are required to have a significant impact parameter with respect to the PV. This helps to remove  $c$ -hadrons combined with an additional track both originating at the PV.

The HLT underwent various improvements between Run I and Run II. The number of CPU cores in the Event Filter Farm (EFF) increased from around 29,000 to 52,000. Most notably the HLT1 and HLT2 components were modified to operate asynchronously. This means during Run II the events passing HLT1 are stored in a temporary buffer (around 11 petabytes in size) to be processed later by HLT2. This allows alignment and calibration to be performed between the running of HLT1 and HLT2. Dedicated calibration samples are produced by HLT1 and processed on the EFF. This includes calculating the VELO and tracking station alignments to optimise the momentum resolution. Additionally, the refractive index of the RICH radiators is calibrated using samples of particles with known masses from specific decays. The

difference in the measured and expected Cherenkov angle is used to determine the required calibration.

These improvements in calibration allow the HLT2 reconstruction to be effectively the same as can be achieved offline. An additional trigger system called the Turbo Stream [15] was added in Run II to create candidates ready for analysis straight out of HLT2. However, candidates analysed in this were processed in the trigger and again offline.

### 3.2.9 Reconstruction

The reconstruction of charged and neutral particles is described in this section.

#### Charged particle reconstruction

Charged tracks are reconstructed using the hits in the VELO, TT, IT and OT. These are classified into different categories depending on their route taken through the detector as shown in Fig. 3.22. The IT and OT are collectively referred to as the T-stations.

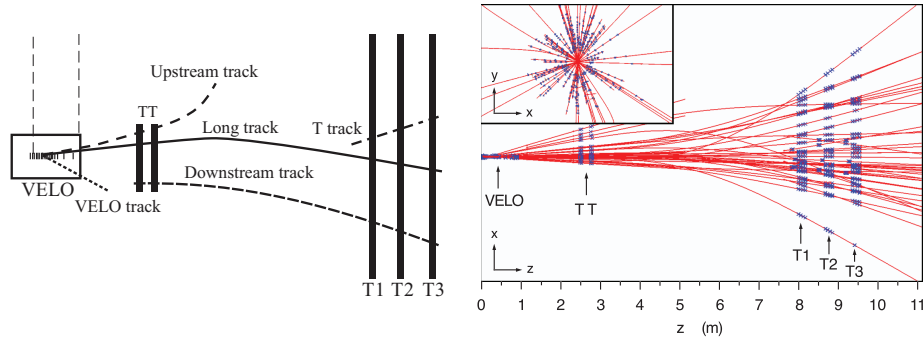


Figure 3.22: Diagram of the different track reconstruction types (left) and an illustration of the reconstructed tracks in a typical event from Ref. [6].

**Long tracks:** these tracks have passed through both VELO and T-stations.

**Upstream tracks:** these only pass through the VELO and TT tracker, not the T-stations. This may be because their momentum is too low so the tracks get bent out of the acceptance in the magnetic field.

**Downstream tracks:** these tracks only contain TT and T-station hits. They provide vital information about long-lived particles that decay after they have traversed the VELO.

**VELO tracks:** these tracks only contain hits in the VELO. They can help improve the primary vertex determination.

**T tracks:** these tracks don't pass through the VELO or TT and are likely to be produced in secondary interaction between the particles and detector material.

The identification of charged tracks used input from the RICH sub-detectors, along side input from the calorimeter and muon systems to identify electrons and muons respectively. As already described in Sec. 3.2.5, the RICH particle identification is performed by comparing the global event likelihood when changing the particle hypothesis. This is combined with information from the calorimeter and muon systems to create an overall particle identification variable

$$\begin{aligned} \Delta \log \mathcal{L}_{\text{comb}}(X - \pi) = & \Delta \log \mathcal{L}_{\text{RICH}}(X - \pi) + \\ & \Delta \log \mathcal{L}_{\text{Calo}}(X - \pi) + \Delta \log \mathcal{L}_{\text{Muon}}(X - \pi), \end{aligned} \quad (3.6)$$

where RICH, Calo and Muon refer to the difference in the log-likelihood of the  $X$  and  $\pi$  hypothesis as determined by the RICH, calorimeter or muon systems respectively.

The calorimeter log-likelihood is constructed by comparing the electron to hadron hypotheses. This uses input from the ECAL, HCAL and PS sub-systems

$$\begin{aligned} \Delta \log \mathcal{L}_{\text{Calo}}(e - h) = & \Delta \log \mathcal{L}_{\text{ECAL}}(e - h) + \\ & \Delta \log \mathcal{L}_{\text{HCAL}}(e - h) + \Delta \log \mathcal{L}_{\text{PS}}(e - h) \end{aligned} \quad (3.7)$$

For the HCAL and PS this input is determined using the energy deposited. For the ECAL this is constructed comparing the ratio of energy to momentum,  $E/pc$ , for the candidates, which peaks around one for electrons and at lower values for hadrons. Additionally, the centre of the ECAL deposit and extrapolated track position are compared.

The muon system log-likelihood is determined by extrapolating the track in question to the muon stations. The average squared distance of the extrapolated positions and hits in the stations are used to compare the muon to non-muon hypothesis.

### Neutral particle reconstruction

The energy of neutral particles are determined directly from the calorimeter system. This system is calibrated during running to maintain the optimal resolution.

**Photons:** Isolated ECAL clusters with an corresponding cluster in the PS are used to create photon candidates. The energy is determined from the total energy deposited in the ECAL and PS.

**Neutral pions:** These mesons decay dominantly to two photons, however the reconstruction depends on the transverse momentum of the  $\pi^0$ . For low  $p_T$  decays the two photons are well separated (*resolved*) leading to two photon deposits. For higher  $p_T$  decays the two photon deposits overlap leading to a single ECAL cluster (*merged*).

**Bremsstrahlung correction:** as a result of their small mass, electrons can radiate Bremsstrahlung photons. If this occurred before the magnetic field the photon produced results in a separate ECAL cluster. If this radiation occurs after the magnet the photon cluster can overlaps with the electron cluster. Clusters in the ECAL that are consistent with radiated Bremsstrahlung photons are used to correct the initial energy of the electron.

## 3.3 Luminosity determination

The observed rate  $R$  of a particular physical processes at particle colliders are defined by the luminosity  $\mathcal{L}$  and the cross-section of the process,  $\sigma$ ,

$$R = \mathcal{L}\sigma. \quad (3.8)$$

Experimentally, the rate of specific interactions are measured, so precise measurements of the luminosity required to determine the corresponding cross-section. Additionally, the total integrated luminosity is useful to understand the size of the data set.

The luminosity can be determined *indirectly*, by reversing Eq. 3.8 and inputting a well-known cross section for a calibration process. Alternatively the luminosity can be determined *directly* by calculating it from the machine parameters. This is determined as follows

$$\mathcal{L} = f_{\text{rev}} N_1 N_2 \Omega, \quad (3.9)$$

where  $f_{\text{rev}}$  is the revolution frequency,  $N_1$  and  $N_2$  are the number of protons in the two beams and  $\Omega$  is a geometrical factor that quantifies the overlap of the two bunches [16]. For two beams of ultra-relativistic particles the overlap integral can be approximated as

$$\Omega = 2c \int \rho_1(x, y, z, t) \rho_2(x, y, z, t) dx dy dz dt \quad (3.10)$$

where  $\rho$  describes the particle density distribution.

Two methods are used to *directly* determine the luminosity at LHCb, described here.

### 3.3.1 Van der Meer scans

The luminosity of the collisions can be determined using the van der Meer technique [17]. This involves sweeping two beams across each other in the transverse plane. By measuring the interaction rate as a function of the beam displacement, the overlap of the two beams can be determined, and hence the absolute luminosity. The two beams are moved simultaneously, alternating between the two transverse directions as shown in Fig. 3.23.

The absolute luminosity is calculated for the specific van der Meer scan fills, and extrapolated to the full data set using the interaction rate of standard processes. The effective visible cross-section  $\sigma_{\text{vis}}$  is calibrated for the standard processes during the

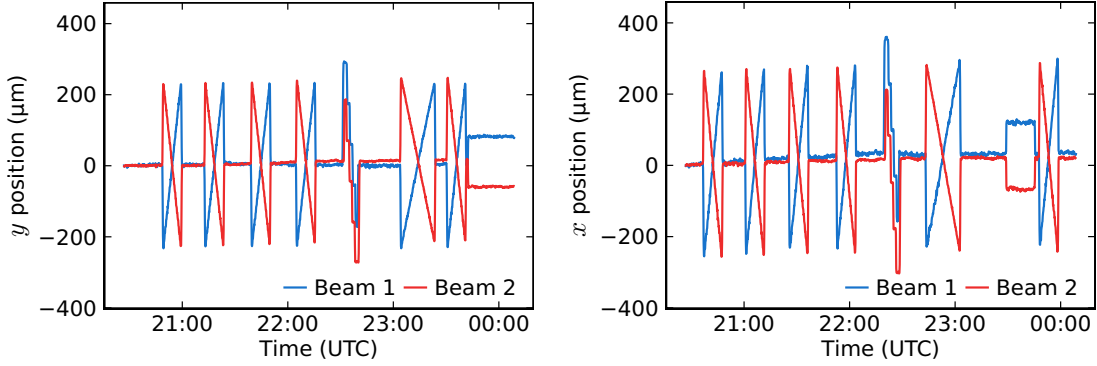


Figure 3.23: Beam positions during a van der Meer scan to determine the absolute luminosity, from Ref. [16].

absolute luminosity determination fill. The total integrated luminosity for a data sample can be determined by the accumulated rate of the standard process.

### 3.3.2 Beam gas imaging

The luminosity can also be calculated by exploiting the interactions between the beams and residual gas molecules in the beam pipe vacuum. The precision of the VELO allows the beam-gas interaction vertices to be reconstructed. These vertices allow the beam position, shape and angle to be determined. The typical distribution of beam-gas vertices in the  $xz$  and  $yz$  planes are shown in Fig. 3.24. The crossing angle in the horizontal plane is clearly visible. The overlap of the two bunches is

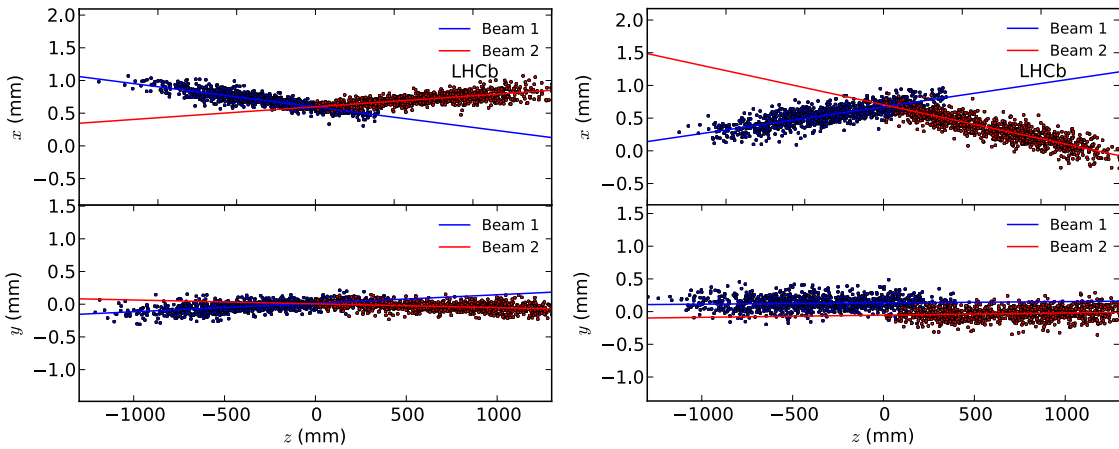


Figure 3.24: The positions of beam-gas interactions reconstructed in the VELO sub-detector, from Ref. [16].

determined by first fitting the beam profiles to obtain the three dimensional density  $\rho(x, y, z)$  for each beam. This is possible due to beam crossings in which only one of the two beams were present. This means all reconstructed beam-gas interactions can be attributed to the single bunch.

### VELO resolution

The distributions of the beam gas interactions as reconstructed by the VELO sub-detector are not simply the beam profiles as vertex position resolution must be accounted for. The resulting distribution is the convolution of the beam profile and resolution distribution. The VELO vertex resolution is strongly dependent on the number of tracks used to create the vertex, as well as the longitudinal position of the vertex.

The resolution of vertices is estimated by splitting the tracks contributing to vertices into two random sub-samples. The vertex position for each of these sub-samples,  $v_{1,2}$  is determined and the difference in the vertex positions  $\Delta v = v_1 - v_2$  is found. The width of the  $\Delta v$  distribution when splitting many vertices is used as a proxy for the resolution. The resolution determined for different values vertex track multiplicity and longitudinal position is shown in Fig. 3.25. These resolution values

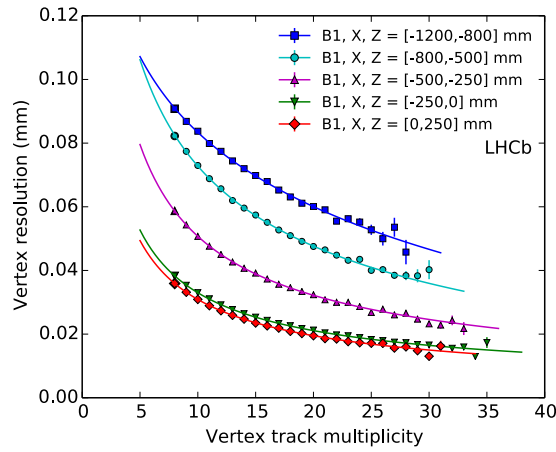


Figure 3.25: The resolution of beam-gas interactions as a function of the vertex track multiplicity and longitudinal position, from Ref. [16].

are used to subtract the smearing from the VELO resolution such that the beam profiles can be accurately determined.

### Real-time beam measurements

The beam gas imaging method additionally allows measurements of the beam profiles to be made in real-time during data taking. As detailed in Sec. 3.1.2 the LHC runs with a smaller number of bunches than the full capacity would allow. The distribution of filled and empty bunch slots are usually chosen to maximise the luminosity for ATLAS and CMS, therefore only a subset of the total bunches collide at LHCb. Those beam crossings in which only one of the two bunches pass through LHCb can be used to make measurements of the beam-gas interactions during normal running. These provide information about the beam angle, positions and shapes. The shape parameters can be used to calculate the emittance of the beams. This information is published back to the LHC, providing important information about the performance of the machine [18].